Key Points:
- Survey of nine separatrix crossings during active reconnection with X-line distance estimated using proton beam dispersion
- Strong Hall-type Ez region overlaps with hot proton beam, hosts Alfvénic E&B variations, intense FACs, cold ions, and strong E fluctuations
- Similar patterns of distant ($>100\ d_i$) and mid-distance crossings (<30–$50\ d_i$) except for their longer duration and larger spatial scales

Supporting Information:
- Supporting Information S1

Correspondence to:
V. A. Sergeev,
victor@geo.phys.spbu.ru

MMS Observations of Reconnection Separatrix Region in the Magnetotail at Different Distances From the Active Neutral X-Line

V. A. Sergeev[1] , S. V. Apatenkov[1], R. Nakamura[2] , F. Plaschke[2] , W. Baumjohann[2] , E. V. Panov[2,3] , I. V. Kubyshkin[1], Y. Khotyaintsev[4] , J. L. Burch[5] , B. L. Giles[6] , C. T. Russell[7] , and R. B. Torbert[3]

[1]St. Petersburg State University, Sanct-Petersburg, Russia, [2]Space Research Institute, Austrian Academy of Sciences, Graz, Austria, [3]Space Science Center, University of New Hampshire, Durham, NH, USA, [4]Swedish Institute of Space Physics, Uppsala, Sweden, [5]Southwest Research Institute, San Antonio, TX, USA, [6]NASA Goddard Space Flight Center, Greenbelt, MD, USA, [7]IGPP/EPSS, University of California, Los Angeles, CA, USA

Abstract The region surrounding the reconnection separatrix consists of many particle and wave transient features (electron, cold and hot ion beams, Hall E&B fields, kinetic Alfvén, LH, etc. waves) whose pattern and parameters may vary depending on the distance from active neutral line. We study nine quick MMS entries into the plasma sheet boundary layer (PSBL) from the tail lobe to address the meso-scale pattern and other characteristics of phenomena for active separatrix crossings as deduced from particle observations. The outermost thin layer (a fraction of ion inertial scale, d_i) of low-density plasma consists of accelerated electron beams and lobe cold ions and displays density depletions (EBL region). It is followed by hot proton beam (PBL region) in which the plasma density grows from lobe-like towards plasma sheet-like values; the beam energy-dispersion is used to estimate the distance from the active neutral line. Thin (usually $\leq d_i$) region containing intense Hall-like Ez perturbations (HR) usually overlaps with EBL and PBL regions. It often includes correlated B perturbations suggesting the Alfvén wave-related transport from the reconnection source; the estimated Alfvénic ratio $\delta E/(V_A\ \delta B)$ varied between 0.3 and 1.3 in studied examples. The HR is associated with profound plasma property changes, including the heating of cold ion beams in its innermost part, it hosts intense structured field-aligned currents and intense E-field fluctuations. Surprisingly, most of abovementioned findings are valid for crossings observed at large distances from the reconnection region (exceeding a few tens Re or $>100\ d_i$) except for longer time-scales and larger spatial scales of the pattern.

1. Introduction

Magnetic reconnection is a fundamental process of fast energy conversion in the plasma which is of universal importance in space plasma. Being a subject of considerable general interest for last decades, the investigation of reconnection process in a near-Earth plasma is currently the main goal of international magnetospheric multi-scale (MMS) mission (Burch et al., 2015).

In the near-Earth plasma environment, the current sheets exist in a variety of different forms, so the manifestations of reconnection display important specific differences. The current sheets at the magnetopause and in the magnetotail are most available for in situ observational study. The magnetopause reconnection regulates the energy flow into the magnetosphere from the solar wind and it has been a primary target of the MMS project during recent years. It includes highly asymmetric conditions on magnetosheath and magnetospheric sides of the sheet with frequent large guide field at the magnetopause, whose combinations result in a variety of reconnection regimes. Quite distinct from that the magnetotail current sheets are symmetric and they are confined between nearly antiparallel magnetic fields of the very diluted lobe plasmas. Due to very large Alfvén velocity in the lobes the tail reconnection is a very efficient particle accelerator which provides fast flows and energetic electron and ion beams.

Reconnection process is characterized by a few structural elements which have important functions and play significant roles in the reconnection process. Particularly, it includes: an electron scale diffusion region where the frozen-in plasma behavior is violated; fast reconnection plasma outflows carrying away the

reconnected magnetic flux, and the intermediate region where frozen-in electrons and unmagnetized ions play together to match the reconnection rate and reconnection outflows. A well-known topological surface, magnetic separatrix, divides open (non-reconnecting) lobe magnetic field lines from already reconnected field lines, in a meridional cut it maps to the X-type reconnection neutral line, XNL. Being magnetically connected with an active XNL region, the region surrounding the separatrix (later referred to as the separatrix region, SR) hosts a number of processes and structures which are in the focus of this study. Different motions of magnetized electrons and non-magnetized ions give rise to intense Hall electric and magnetic fields in the intermediate region surrounding the XNL (Eastwood et al., 2010; Nagai et al., 2003; Øieroset et al., 2001). Being formed in relatively small region of ion inertial scale, these fields may be expected to propagate along magnetic field lines over large distances near separatrix, particularly as Kinetic Alfvén waves (Chaston et al., 2009; Dai, 2009; Dai et al., 2017; Shay et al., 2011). The energetic particles accelerated in the diffusion region may also propagate outward along magnetic field lines near the separatrix as energetic particle beams. Significant field-aligned electric fields are formed in the SR which force electrons to move toward the reconnection site, forming inward-moving (toward XNL) electron beam which also provides a part of Hall current loop system responsible for the quadrupole magnetic field (Hesse et al., 2016; Paschmann et al., 2013). Also the energetic particle beams and strong gradients of particle distributions in the separatrix region give rise here to a rich variety of instabilities and a wealth of waves (e.g., Khotyaintsev et al., 2019). Cold ions of ionospheric origin are also an important part of the story as they are abundant in the lobes, penetrate inward across the separatrix and may influence the plasma dynamics and generation of instabilities (e.g. Alm et al., 2018; Khotyaintsev et al., 2019).

The structure of entire reconnection region briefly mentioned above, has been established in numerous particle-in-cell (PIC) kinetic simulations, which provide the contemporary detailed understanding of the reconnection process (e.g. Hesse et al., 2016; Lapenta et al., 2016; Shay et al., 2011). However, usually such simulations are performed for the 2D systems, use idealized setups and have some other limitations (like unrealistic mass ratio of ions/electrons), so they need an observational verification. Also, because of relatively small size of simulation domain and relatively short simulation time it is hard to explore the reconnection phenomenology at large distance from time-varying reconnection region, where different components (particles and field structures) may arrive at different times and where the perturbations interact with the closed plasma tubes in the near-Earth region.

Many of abovementioned elements of tail reconnection picture have been also confirmed in spacecraft observations (e.g. Øieroset et al., 2001; Nagai et al., 2003, 2015; Eastwood et al., 2010; see also a review of pre-MMS results in Hesse et al., 2016; Paschmann et al., 2013). The observations still provide a rather fragmentary view because of single-point nature of observations, difficulty of separating spatial/temporal effects and, in most cases, availability of only local observations in single particular events. Even more they suffer from instrumental limitations, including insufficient time resolution and, especially, rare availability of a comprehensive set of basic characteristics including electric currents, plasma and field gradients, 3D convection, etc. The latter problems are mostly resolved in the currently active MMS mission which provides an attractive possibility for detailed study of the tail reconnection taking into account its superior orbital, instrumental and multi-spacecraft capabilities. We use them in this study to survey the structure of reconnection separatrix region (SR), and address its scale-sizes and variability with the emphases laid on the SR patterns and distance dependence of SR appearance. An additional motivation is that spacecraft crossings of reconnection separatrix are much more frequent than crossings of the diffusion region, so they may provide an attractive possibility for reconnection monitoring.

Based on topological reasons, in most cases magnetic separatrix in the magnetotail is thought to be associated with the outer part of the hot plasma sheet, the plasma sheet boundary layer (PSBL). The PSBL is known by its complicated kinetic features, frequent appearance of uni- and bidirectional beams of charged particles having both magnetospheric and ionospheric origins, as well as by its rich spatial and/or temporal structure (e.g., Parks et al., 1998). Statistically (e.g., Walsh et al., 2011) this region manifests bidirectional electrons and unidirectional Earthward high energy ion beam of (tens keV ions) at the outer PS edge which changes to bidirectional distribution deeper inside, before finally changing to the isotropic ion distributions in the central plasma sheet. Establishing that reconnection is going on during PSBL observation and evaluation of the distance to the reconnection line—these are non-trivial tasks to solve when studying the reconnection separatrix region. Fortunately, some particle observations can assist to accomplish this task.

A notable feature often observed during quick crossings of lobe-PSBL boundary is that a few hundred eV lobe electron population (known as polar rain, PR) is replaced by accelerated electrons prescribed to the action of reconnection process, with a well-defined flux gap between these two populations. Such observations are available both in the tail and at low-altitude spacecraft, e.g., Alexeev et al. (2006), Shirai et al. (1997), and Varsani et al. (2017). Also, at such times there are indications that electron edge of the PSBL lies lobeward of the ion edge and that their distribution has low energy cutoffs (LECs) varying in time, similar to the proton PSBL picture (Onsager et al. 1990), however very high temporal resolution is required to observe such an electron dispersion in the PSBL (Varsani et al., 2017). The long-known (since Takahashi & Hones, 1988) energetic proton beam at the plasma sheet boundary, which manifests the energy dispersed LEC feature (with less energetic particles arriving later), provides another potential indicator of active reconnection. Such dispersion is interpreted as being due to the differences of particle time-of flight (TOF) from the acceleration source (XNL) to the observation point, $t_{TOF} = L/Vp$, where L is a distance and Vp is the particle velocity (Onsager et al., 1990). Such energy dispersion can be formed in two ways, both of which have an observational support. The temporal dispersion is valid in case of impulsive reconnection and step like flux increase of all particle energies at the source (e.g., Birn et al., 2020). Such multiple minute-scale energy-dispersed proton beams are observed at mid altitude spacecraft above the substorm auroral bulge (Sauvaud et al., 1999). The spatial dispersion (or velocity filter effect) originates even under the stationary reconnection, because the particles accelerated at the reconnection site move out along the flux tube at their velocities Vp and arrive to the observing spacecraft after different times equal to their flight times (t_{TOF}). Since this flux tube is displaced from separatrix inward (into the plasma sheet) by the convection, in case of active reconnection the particles forming the low energy cutoff will be displaced inward according to their t_{TOF}, providing spatially dispersed LEC pattern. Again, spatial dispersion is easier to observe at low-altitudes where it provides the well-known velocity-dispersed ion structures (VDIS) near the polar cap boundary (Zelenyi et al. 1990), as different from temporal-dispersed structures TDIS (Sauvaud et al., 1999). Studies of ion dispersion origin in the PSBL using Cluster data showed that transient ion injections are often embedded into a broad region corresponding to the latitude-dependent convection-filtered energy variation (Keiling et al, 2004; Sauvaud & Kovrazhkin, 2004). Quantitative interpretation of proton energy-dispersed LEC features provides a possibility of getting some estimates for the distance to the acceleration source (in our case—reconnection site location), although the velocity filter-based interpretation was not massively applied in the magnetotail studies so far. Extending the analyses made by Varsani et al. (2017), here we use the proton dispersion to get the estimates of the XNL distance. More detailed description of the simple method taking into account the spatial energy-dependent dispersion is presented in Wellenzohn et al. (2020) (see also Supplement 1).

As follows from this introduction, there is a need of systematic study of the PSBL structure in reconnecting plasma sheet for many events, in which reconnection in progress can be confirmed and distance from active reconnection can be evaluated. MMS observations provide the most attracting possibility of such study taking into account their superior instrumental and multi-spacecraft capabilities. Particularly, the burst mode operation is essential for crossings made close to the XNL, whereas fast mode operation can also be useful for distant crossings. Here we survey nine those PSBL crossings from lobe into the plasma sheet on the Earthward side of the XNL during which the active reconnection can be evidenced by particle signatures of reconnection. We do not request to cross deep into the CPS, as this usually requests several minutes during which a few reconnection pulses can occur. Being focusing on mesoscale features, which are seen at 1 s time resolution, we are interesting to establish the patterns and characteristic scales and amplitudes of the above-discussed phenomena.

2. MMS Observations and Data Analyses

Below we show MMS observations during a few events with the purpose to illustrate the identification of active reconnection events, as well as to show typical features of the separatrix region and the methods used to evaluate the distance to the reconnection line and reconnection rate. Following Retinò et al. (2006) under the name "separatrix region" we identify the entire region between lobe/plasma sheet interface and well-developed reconnection outflow. The plasma distributions and moments are from the Fast Plasma Investigation (FPI, Pollock et al., 2016), the electric field and spacecraft potential are from the Electric field Double Probes (EDP, Ergun et al., 2014; Lindqvist et al., 2014), and the magnetic field is from the FluxGate

Magnetometer (FGM, Russell et al., 2014). All vectors are given in Geocentric Solar Ecliptic (GSE) coordinates. During tail seasons of years 2017 and 2018 the typical inter-spacecraft distance in the near-apogee part of MMS orbit was about 20–40 km. Generally, the availability of burst mode was required to process the energy dispersion for most of events (with 30 ms and 150 ms time resolution for electrons and protons, correspondingly), however, the events showing a long (minute-scale) ion energy dispersion could well be processed using the fast mode plasma data. Fast mode data from FGM (16 Hz) and EDP (32 Hz) are used in all events to compute 1s averages used to characterize their mesoscale structure.

We first present in the Section 2.1, the observations made close to the reconnection line, then show two examples of most distant reconnection events (Section 2.2) and then discuss the middle-distance events (Section 2.3). For simplicity, all events for our study are selected on the Earthward side of the reconnection line (XNL) where the crossing of lobe-plasma sheet boundary most probably indicate the crossing of reconnection separatrix and the active stage of reconnection process can be established by observing Earthward proton beam, its energy-dispersed Low Energy Cutoff as well as the polar rain (PR) electron gap (the gap in the higher energy part of PR electrons population at energies 100–300 eV), see e.g. Varsani et al. (2017).

2.1. Examples of MMS Crossings Close to the Reconnection Line

Three abovementioned particle reconnection signatures are clearly seen in two events presented in Figure 1. Being observed at points [−22.1; −5.1; 3.6] R_E and [−22.8; −8.8; 5.2] R_E GSE in the tail, they occurred near the peak of AE ~400 nT substorm and at the beginning of AE index increase, correspondingly. As follows from electron spectrogram (panel c1), in event 1 four spacecraft visited the lobe for the short time (after 1937:53 UT) when only PR electrons are seen. PR electrons disappear at 1938:20 being substituted by accelerated (a few keV) electrons. Shown by dotted red line in Figure 1, 1938:20 UT in event #1 and 0921:30 UT in event #2 are the suggested times of magnetic separatrix crossings. Based on observations alone, the portion of separatrix surface closest to the reconnection line can be recognized by observing the energetic electron fluxes directed toward the XNL (Nagai et al., 2003), that is tailward electron beam in our cases. These events are also characterized by short duration of the energy dispersion of Earthward proton beam, which continues for 10–15 s in panels a. According to pitch-angle (PA) spectrogram in panel b, the tailward electron beams are sporadically seen during ~20 s in event #1 (note, in this case the spacecraft was in the southern lobe and tailward beams are seen as flux enhancements near 0° PA) as well as during 9 s in event #2 (here, in the northern hemisphere, the flux enhancements are seen at 180° PA).

The electron moments are not very accurate in the low-density (lobe-like) region where many data points in the FPI moment time series are missing and many other data points are flagged as unreliable ones for densities of 0.05 cm^{-3} or less. Being interested to keep as much information in these low-density regions, in the burst mode we processed all data irrespective of flag values by accumulating 33 subsequent measurement points (which correspond to 1 s-long interval in case of no data gaps) and finding the median value of each parameter.

An appropriateness of these processing efforts in the lobe-like low-density regions is illustrated by Figures 1d, 1e, and 1f. First of all, we find a good consistence between moment values obtained at all four spacecraft (only data from M1 and M4 are shown here). Second, in this case, no ASPOC potential control was applied and spacecraft potential can be used for semi-quantitative control of derived densities. Indeed, a good anticorrelation between Log Ne and spacecraft potential is obvious between panels f and g, and the range of values (35–40 V potential for 0.03–0.05 cm^{-3} densities) is usual for such low-density plasma (e.g., Haaland et al., 2017). A similar correspondence is also seen in the event #2 for spacecraft M4 (red curve) which had no potential control. Third, the electron velocity is known to be most noisy of all moments, and its independent test is of a great value. In the panel e, we compare the electron Vex component with the jx component of the electric current derived by the curlometer method from magnetic observations made on four MMS spacecraft. In the outermost part of separatrix region, where electron beams exist in the absence of energetic protons and where electrons can provide an important contribution to the current, we expect to see an anticorrelation between Vex and jx. On panel e the axes directions on the right and left sides are inverted and their scales are adjusted so (being 10 [nT/1,000 km] for 1,000 km/s) that Ve variation should correspond to jx variation for densities of 0.05 cm^{-3} in case of pure electron current. Indeed, the expected anticorrelation for large-amplitude Vex and jx variations is observed in the separatrix region which appear
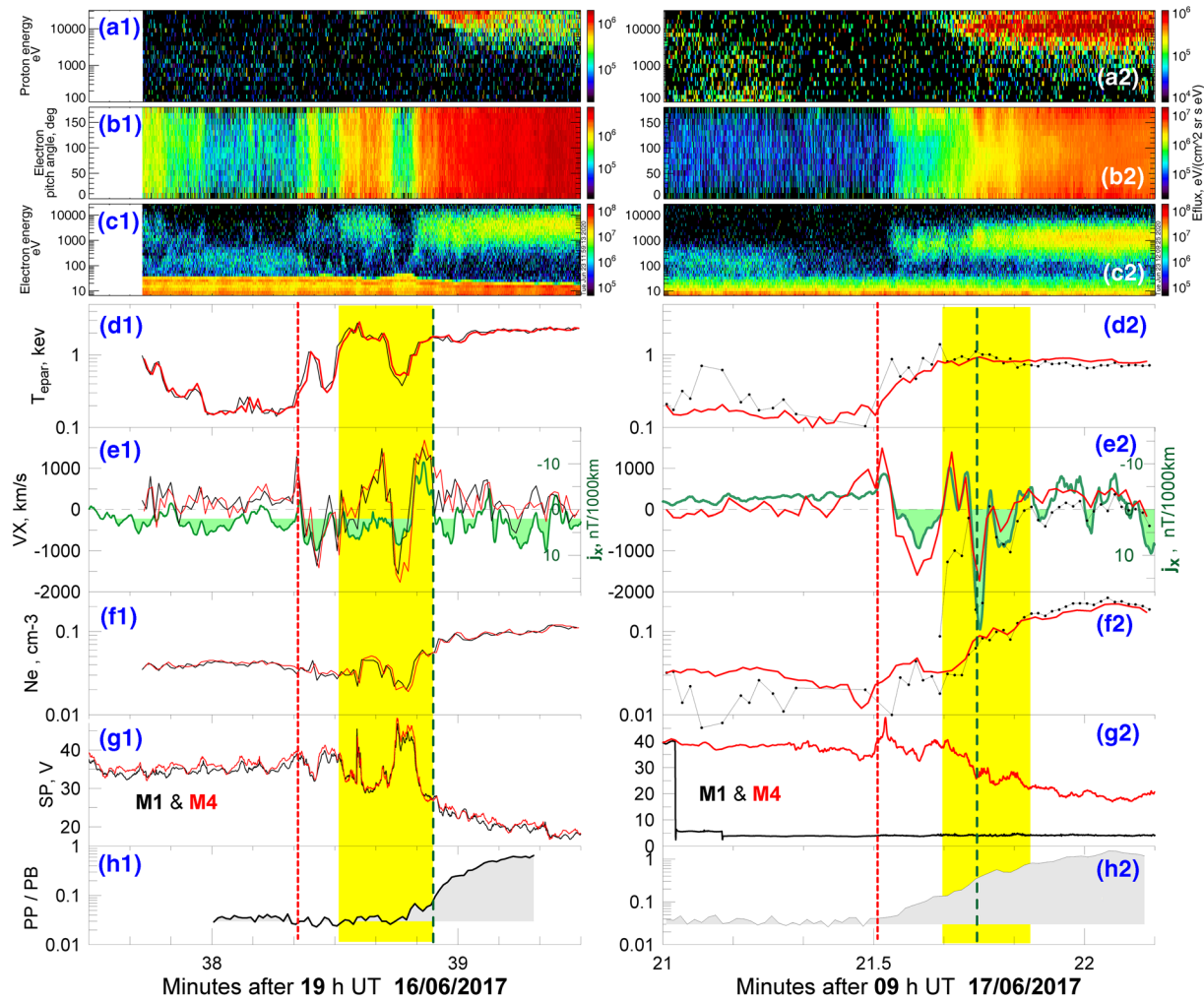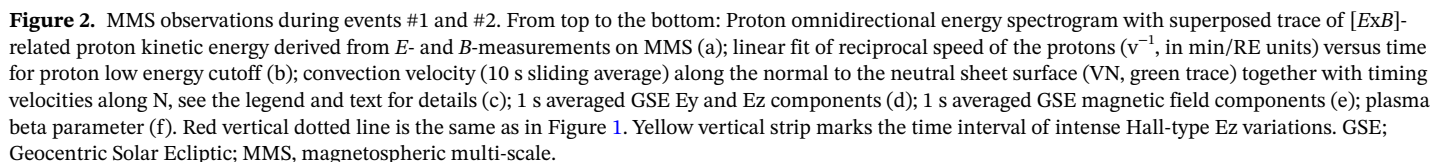
Figure 1. MMS observations during PSBL crossings #1 (left) and #2 (right). From top to bottom: Energy spectrogram for the Earthward streaming protons (a); pitch-angle spectrogram of electrons above 2 keV (b); energy spectrogram for the Earthward electrons (c); parallel Te (d); Vex and jx variations (e, note that jx axis direction is inverted); electron density (f); spacecraft potential (g); plasma beta (h). Vertical dotted red line indicates the first appearance of accelerated electrons, green dashed line shows the start-time of thermalization of the cold ion beams (see below). Note that e-velocities at M1 (black trace) in panel e2 are not shown in low-density region before 0921:37 UT, because their median values were unrealistically small, l below −3,000 km/s. MMS, magnetospheric multiscale; PSBL, plasma sheet boundary layer.

in the central part of these panels, especially in the event #2. (Unfortunately in event #1 the curlometer data suffer from some contamination manifested as ∼20 s spacecraft spin tone seen at the beginning of interval). This helps us to believe that the Vex variations derived from flagged FPI data in the low-density region provide useful data for analyses for measurements in which the potential control (ASPOC) is applied, like for MMS1 in event #2, the situation differs. In those cases, the amount of FPI moment data points with missed data usually increase and median Vex values for remaining low-density flagged data are systematically shifted down to big negative values (well below −2,000 km/s), indicating that the processed velocity data are unusable. This was the case for many events in 2017 and, especially, in those selected in 2018. We have no explanation for such ASPOC action. On the other hand, in these conditions the electron density and temperature values are comparable between different spacecraft and we still use them thereafter to characterize the low-density regions.

After making these methodical remarks, a few important properties of the separatrix region can be inferred from Figure 1. First, the outer layer of separatrix region (which continues about 30 s and 20 s in events 1 and 2) contains strong pulses of negative Vex and positive jx (downward FAC), which are interpreted as manifestations of tailward electron flow bursts or beams. During that time the electron density does not

Figure 2. MMS observations during events #1 and #2. From top to the bottom: Proton omnidirectional energy spectrogram with superposed trace of [*ExB*]-related proton kinetic energy derived from *E*- and *B*-measurements on MMS (a); linear fit of reciprocal speed of the protons (v^{-1}, in min/RE units) versus time for proton low energy cutoff (b); convection velocity (10 s sliding average) along the normal to the neutral sheet surface (VN, green trace) together with timing velocities along N, see the legend and text for details (c); 1 s averaged GSE Ey and Ez components (d); 1 s averaged GSE magnetic field components (e); plasma beta parameter (f). Red vertical dotted line is the same as in Figure 1. Yellow vertical strip marks the time interval of intense Hall-type Ez variations. GSE; Geocentric Solar Ecliptic; MMS, magnetospheric multi-scale.

increase and, instead, at 1938:35 and 1938:45–50, we observe significant density drops, by a factor 2 against the lobe values. The density depletions in event 2 are observed near 21:30 and 21:40 UT, being also visible as the peaks of spacecraft potential recorded at MMS4. Strong correlated pulses of negative Vex and positive jx peaked at 0921:37 and 0921:44 (*e2*) are clearly associated with tailward beams of keV electrons seen on spectrogram (*b2*) seen on top of isotropic electron background. Considerable increase of the electron density starts nearly with the appearance of proton beam, at around 1938:50 in event 1, and after 0921:43 in event 2. Parallel electron temperature reaches its maximal values in the low-density region, it does not show any significant increase afterward, after the full development of the dispersed proton beam. So, the outermost part of separatrix region can be described as the low-density high-energy electron beam region where significant localized tailward electron beams and associated localized Earthward field-aligned currents do occur.

More information about proton characteristics and electromagnetic field is available from Figure 2. For the stage of energy-dispersed proton beam, in panel *b*, we analyze the dependence of low energy cutoff (LEC) in coordinates–reciprocal velocity (1/V) versus time, where $V = (2W/m)^{1/2}$ is the velocity of particle having the mass *m* and energy *W*. To determine LEC we averaged over 1 s intervals the proton spectra taken within 30° of Earthward direction and usually chose the threshold energy flux values being a factor 5 above their average values in the lobe region. We did this for each spacecraft separately and plot in panel *b* the results for MMS1 and MMS2 together to increase the statistics. As discussed in the Section 1, such presentation refers to the time-of-flight (TOF) equation $t = L/V$ for particles accelerated in the same region (presumable, near the XNL) and propagated over the distance *L* to the spacecraft location at the velocity *V*. As follows from

linear fit of data points, the TOF-based distance estimates give LTOF = 3.2 R_E (*b1*) and 2.4 R_E (*b2*) as well as apparent injection times about 1938:38 and 0921:27 UT, correspondingly.

Another important detail concerns the presence of cold ions (CI) which are seen as the narrow trace in low energy part of omnidirectional spectrogram on panel *a* in Figure 2. These CIs are ordinary in the lobes (see Alm et al., 2018; Varsani et al., 2017, etc. for MMS observations). On panel *a* their energy varies similar to the white line on the spectrogram, which shows the changes of the kinetic energy of proton convective motion m $VE^2/2$, where $VE = [E \times B]/B^2$ is the convection velocity computed from magnetic and electric field measurements at the MMS. The CI narrow traces are nicely seen throughout the outer part of electron separatrix region during 35 s (*a1*) and 13 s (*a2*). At the times shown by green dashed lines, the narrow trace spreads toward high energies and join the hot beam population, signaling on heating of cold ion beam. This occurred at the start (*a1*) or near the end (*a2*) of energy-dispersed part of energetic proton beam signature.

Mesoscale magnetic and electric field variations at 1 s resolution are shown in panels *e* and *f*. Major magnetic field signature of PSBL entry is the drop of magnetic field magnitude (Bx) and associated increase of plasma beta parameter, manifesting the entry into the plasma sheet. Major electric field signature in the separatrix region is the large-amplitude Ez variation (peak amplitude 19 mV/m and 10 mV/m, correspondingly) which is positive in the southern PSBL (*d1*) and negative in the northern PSBL (*d2*); note that the directions of *E*-axis are opposite in two events to facilitate visual comparison of PSBL crossings made in two hemispheres. Such direction of strong vertical electric field, toward the neutral sheet, corresponds to the direction of reconnection-associated Hall electric field. Yellow vertical strip marks the time interval of intense Hall-polarity Ez variations, thereafter we shall refer to such intervals as Hall regions (HR). These variations are also accompanied by correlated By-component variations, being negative (positive) in southern (northern) PSBL crossings. These polarities correspond to those of quadrupole Hall-type magnetic fields associated with reconnection. The magnetic field magnitudes are rather small, a few nT, but this is roughly what is expected in case of Alfvénic nature of these variations. Numerically, for the local Alfvén velocity of 2,400 km/s (for $n = 0.04$ cm^{-3} and $B = 22$ nT) the expected magnetic perturbation would be about 4 nT if electric field variation is 10 mV/m. In the second event, By perturbations are very small and they are hardly seen on top of large, gradual, 30 s-long By increase (such feature was not typical among the events in our study).

In both events during considerable part of the PSBL crossing the Ey component was negative indicating the outward (lobeward) motion of the plasma tubes or, equivalently, the spacecraft motion into the plasma sheet. At first glance this is opposite to the inward convection of reconnected plasma tubes expected in the standard reconnection cartoons. However, the true motion of the separatrix is of large importance. We expect to get some estimate of actual separatrix motion using inter-spacecraft timing of magnetic field time-series measured by four FGM instruments as previously described by Plaschke et al. (2016). In its original version (labeled by index P below), the cross-correlation of magnetic fields in all three components was performed between pairs of MMS spacecraft after subtracting the component mean value in the sliding window (this may diminish, for example, the influence of offset problems). In another version of timing, we do not subtract the mean values and cross-correlate the original GSE magnetic field components when minimizing the RMS of component differences at spacecraft pairs (this may help to emphasize the contribution of regular *B*-gradients in the current sheet, this version is labeled by index A). Normally the results depend on the width of time window. Examples of timing velocities (VT) for time window width 10 s using both methods are shown in panels 2*c*, together with properly averaged convection velocity (VE). In this panel, we only compare the 'normal' components of these motions which are of primary interest for us. The normal direction (N_{cs}) was determined by finding the normal to the neutral sheet (Bx = 0) surface of empirical magnetic configuration as given by the recent model TA15 (Tsyganenko & Andreeva, 2015). This model takes into account different kinds of surface deformations for the particular epoch and solar wind state. The normal vectors are shown on the panels by the green fonts.

In both events, the timing velocities are small before the separatrix crossing time and increase in lobeward direction near that time. Afterward most of time where two methods VTp and VTa show similar values, we often have VT > VE indicating that plasma is convected inward across the magnetic gradient region which is expanding outward against the plasma. This is consistent with the reconnection scenario. The difference VT-VE amounts up to 100 km/s, with $B = 22$ nT this means ~2 mV/m, a quite reasonable estimate for peak reconnection rates.
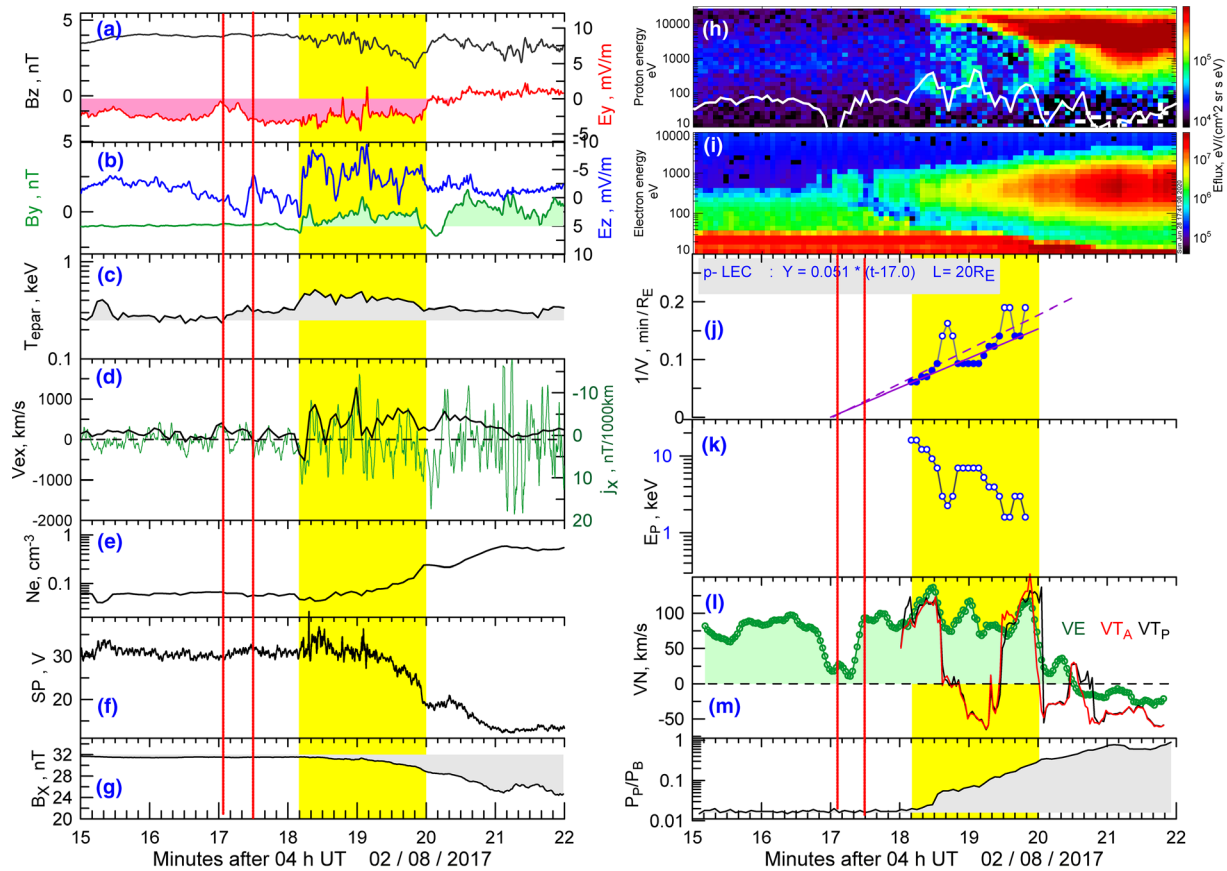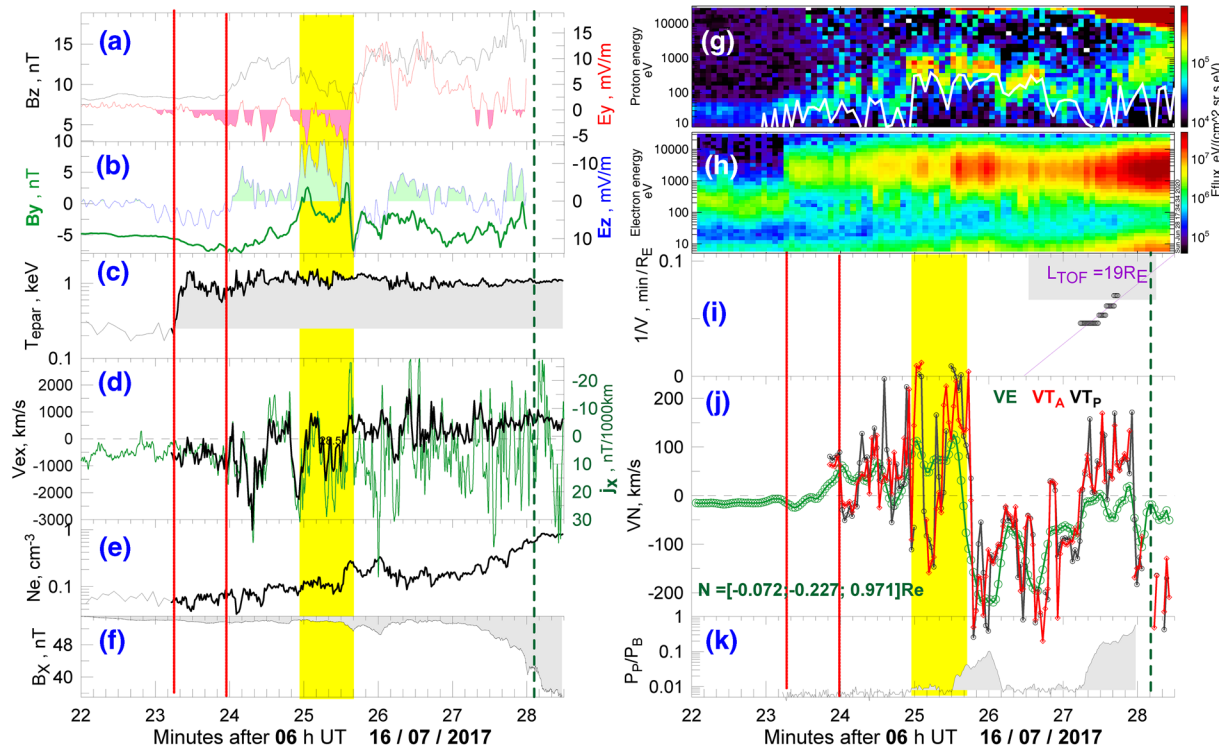
Figure 3. MMS observations during remote distance event #9 in the northern PSBL. From top to bottom, on the left side: Bz and Ey (a), By and -Ez (b); parallel Te (c); Vex and -jx (d); Ne (e); spacecraft potential (f); Bx-component (g). On the right side: proton omnidirectional energy spectrogram with superimposed trace of [ExB]-related proton kinetic energy (h); electron spectrogram (i); linear fit of reciprocal velocity versus time for the proton low energy cutoff (j); energy variation of proton beam low-energy cutoff (k); normal components of convection (VE) and timing (VT) velocities (l); plasma beta parameter (m). Double onset of accelerated electron beam is shown by red vertical dotted lines; yellow vertical strip marks the time interval of intense Hall-type Ez variations. MMS, magnetospheric multi-scale; PSBL, plasma sheet boundary layer.

2.2. Two Examples of Distant Crossings

The PSBL crossing shown in Figure 3 (event #9 in the event list) visually shares many of the features previously seen in Figures 1 and 2, although its time-scale is a few times longer, indicating a longer energy dispersion time-scale and, presumably, longer distance to the XNL. It was observed at $[-13.7; -0.1; 4.5]\ R_E$ during geomagnetically quiet period. The signatures of accelerated electrons at energies above the polar rain population and PR gap formation are clearly seen in fast mode electron spectrogram in panel (i) since ~0417:00 and repeat again at ~0417:30 UT. The burst mode started after 0417:51 UT. A special feature of this event is almost steady negative Ey ~ −2. −3 mV/m (panel a) and corresponding lobeward convection of the plasma tubes at velocity 80–100 km/s which is observed between 0411 and 0420 UT.

Before 0419 UT the electron density is low (e) and spacecraft potential is large-(f) with indications that electron density dropped down by a factor 2 below its lobe values between 0418 and 0419 UT. Maximal parallel energy of accelerated electrons ~500 eV was attained at ~0418:20 (c), such rather low value is typical for distant reconnection events observed tailward of lunar orbit (Grigorenko et al., 2019). Energy-dispersed energetic proton beam developed since 0418:10 UT (h) and the gradual increase of electron density was observed (e). Intense Hall-polarity (negative) Ez with approximately correlated Hall-polarity (positive) By (panel b) started at around 0418:10 and continued for 2 min. Like in Figures 1 and 2 the HR time interval is marked by the yellow vertical strip. In this case intense Hall-type signatures started together with the first appearance of dispersed proton beam. Some anticorrelated weak Vex and jx variations are observed since the first appearance of accelerated electrons (panel c), but their amplitude obviously intensified during the first

Figure 4. Similar to Figure 3 but for MMS observations during remote crossing #8 of the northern PSBL on July 16, 2017. MMS, magnetospheric multi-scale; PSBL, plasma sheet boundary layer.

half of "yellow" interval. Faint traces of cold ions have also been observed on omnidirectional spectrogram (panel *h*) till 0419:55, then their trace widened, merged to the main population and was not seen anymore.

As regards the Earthward field-aligned current jx component (panel *d*), its pulses are frequently seen during and after the yellow-coded interval. Different from events 1 and 2, a noticeable tailward electron flow pulse (−520 km/s) was recorded only once, at the beginning of HR.

Magnetic field gradients and variability are low before 0418UT. After that time both timing methods (used with 10 s sliding window) show consistent results (panel *l*). During two intervals, between 0418:00–18:30 and 0420:30–21:00 UT the timing velocities are positive and stay close to VE values, about 100–120 km/s, but no systematic difference of VT > VE sense is obvious, indicating that reconnection rate can be low and poorly defined by the data available. In between these two intervals, the timing velocity dropped below zero, we have no obvious interpretation of this observation. After 0420 UT, both the convection and timing velocities drop to low values, at that time the spacecraft is already very deep in the plasma sheet, plasma beta is above 0.3 and continues to increase (*g*).

The energy dispersion seen at the proton spectrogram (*h*) was processed to identify the low energy cutoff, its variations are shown in panel (*k*) by the blue symbols. If we ignore two large surges, in reciprocal velocity plot (*j*) one can derive the linear regression corresponding to the source distance being $20R_E$ tailward of spacecraft. In fact the distance correction factor (∼VT/(VT − VE), see Equation S4) should be large, although its value cannot be accurately determined in our case. Another way is to use in similar way the energy-dispersed upper energy cutoff of polar rain electrons (panel *I*), which is shown by red points in panels *j*,*k*), which gives 120 R_E distance estimate. Anyway, both estimates indicate the reconnection being in the distant tail, consistent with relatively low energy of accelerated electrons.

In Figure 4, we present a more complicated PSBL crossing with a long energy-dispersed proton beam signature, which occurred during the early phase of AL ∼ 450 nT substorm commencing at ∼0605 UT, the MMS was that time at [−15.7; −3.3; 4.9] R_E. Displaying a more intense manifestations, it is also interesting because the spacecraft has spent a relatively long time, about 2 min, in the outer electron layer of separatrix

region. Burst mode was switched on at 0623:13 UT. The Earthward-directed keV electron beam suddenly started at 0623:16 UT (panels *c, h*), the reflected e-beam appeared 3s later and the gap between accelerated and PR electrons was soon formed (*h*). Until the first contact with the proton beam at ∼0625:30, for about 2 min, the MMS stayed in the low-density region (*e*). Here intense bursts of positive field-aligned currents jx transported by fast tailward electron flows with magnitudes up to 2,000–3,000 km/s (*d*) are observed. Indeed, the quantitative agreement between Vex and jx variations is remarkable in panel *d*. The HR region is very pronounced either. Although it may be defined differently, here we marked the most intense part of perturbations between 0623:55 and 0624:35 UT where most intense negative Ez (down to −15 m*V/m*) and correlated sharp features of positive By variation are observed (*b*). This HR stays outside but adjacent to the dispersed proton beam time interval. Also one may notice two other approx. 1 min long regions of enhanced negative Ez (after 0624 and after 0626 UT) which *were not* accompanied by correlated By signatures.

Before 0625:40 Ey is predominantly negative (*a*) which explains progressive outward motion of PSBL region traversed by MMS, as reflected by strong positive VN in panel *j*. After that time Ey is large and positive for a couple minutes, the inward plasma tube motion was probably the reason why the entry to the proton beam was interrupted for a minute. The distance estimates are possible only during the second encounter with the hot proton beam after 0627 UT. The uncorrected TOF estimate gives roughly 19 R_E (panel i). Independent evaluation of accelerator distance in this event by Birn et al. (2020) gave 25 R_E (see their Figure 3). Anyway, the long residence in the eSR region together with source distance estimate agree that the reconnection region was rather far from the MMS, >20 R_E in this case. Cold ion beam trace has been continuously observed in the lobes and throughout most of PSBL region, signature of its heating was noticed as late as at ∼0628:10 UT.

Magnetic field gradients and variability are low before 0623:50 UT. After that both timing methods in panel (j) (10 s time window results) show similar behavior of normal component of the timing velocity, which is generally consistent with the overall convection changes. However, the scatter of individual points is large which makes difficult the quantitative interpretation of VT and VE differences. During the time period of energy-dispersed proton beam the relationship between velocities is such that VT > VE, indicating that plasma is convected inward across the magnetic gradient region consistent with the reconnection picture. The difference VT–VE amounts up to 100 km/s, with B = 53 nT this means ∼5 m*V/m*, a high but reasonable rough estimate for the peak reconnection rate during substorm activity.

2.3. Survey of MMS Mid-Distance Events. Alfvénic Test

Here we first provide a quick survey of burst-mode observations made during four active PSBL crossings to demonstrate some repeated features and notice their variability. All four events (##4–7) are northern hemisphere active PSBL crossings, which can be classified as middle-distance events in our collection. Short time interval between electron and proton beam onsets, confirmed by the distance estimates given below, indicate that they are observed, say, at ΔX ∼ 5–10 Re from the source. On the other hand, different from events #1 and #2, they started from observing the Earthward electron beam followed 2–3 s later by the reflected electrons, so in these events no energetic e-beam toward the XNL (no Hall-loop electrons shown in reconnection cartoons) was observed near the separatrix.

The FPI temperatures are shown in the row *b* for protons (red) and electrons (black). The proton bulk flows are shown in row (*a*) with j_X (green) superposed onto the proton Vx to characterize the field-aligned current and electron flow contribution to it. The electron flow observations were corrupted in the low-density regions of year 2018 events, as already discussed in Section 2.1. The next row (*c*) characterizes the short duration electric field variability over 1 s time interval calculated as $\delta E = ((Ex^{max} − Ex^{min})^2 + (Ey^{max} − Ey^{min})^2 + (Ez^{max} − Ez^{min})^2)^{1/2}$ from 32 Hz E-samples; it allows to visualize the LHD wave activity and (to some extent) E-field spikes related to e-holes.

Two next panels (*d, e*) provide information about up-down motions of PSBL plasma tubes in the direction normal to the neutral sheet surface (N_{cs}). Similar to previous figures, they include the sliding 10−s averages of the normal component of both convection flow ($VE_N = N_{CS}*(E × B)/B^2)$) and timing velocities VT (using two modifications discussed in 2.1 and E averaged over 4 spacecraft). Timing results are not shown for small magnetic field difference values which are below 0.1 nT/1,000 km. In panel *d* we show the integral value $\Delta ZN = \int VE_N \, dt$ which helps to characterize the spatial scales of structures along the normal.

The bottom block (panels *f, g, h*) presents the 1 sec-averaged electric and magnetic fields in the format which helps to visualize the anticorrelation between Ez and By and correlation between Ey and Bz, which are expected in Earthward-propagating Alfvén waves. As before, the Hall-type regions (HR) are highlighted by yellow vertical strips. We caution that Ez-component (and, to a lesser extent, other *E*-components) sometimes suffers from spacecraft charging and wake effects, especially in the low-density regions. Event #4 provides an example of such strong interference: it occurs at the beginning of event (and highlighted by blue shading), being manifested as clear spin tones in Ez and δE traces which have different phases at different MMS spacecraft (not shown here).

The proxy of magnetic separatrix crossing, the times of e-beam onset, were determined based on electron spectrogram (not shown here), it is marked by vertical red dotted line in the Figure. As seen in panel (*b*) in most cases the electron Tepar increases at around this time, and sharp increase of the proton temperature is delayed by 15–30 s. The Tp increase is actually due to the growth of energy-dispersed hot proton beam superposed onto the cold ion background. Like it has been already noticed in Figures 1–4, the peak values of Tepar are observed in the first half of yellow-shaded intervals, near the start of Tp increase (#4, 6, 7) or during the gradual Tp increase (#5). In all cases Te decreases after the Tp reaches its maximum. It is remarkable, that peak values of Te and Tp are comparable in the magnitude in the separatrix region, whereas at the end of the interval Tp/Tepar approaches 3–5, being closer to the typical plasma sheet values (Walsh et al., 2011). The average proton velocity Vpx (panels *a*) also reaches its peak (here in the range 300–600 km/s) by the end of yellow strip, suggesting that here we enter into the fully-developed reconnection outflow.

Similar to events in Figures 3 and 4, there are only faint prints of field-aligned current at around the e-beam onset. After well-defined pause of 10–30s duration, the major FAC variations start as the positive jx pulse (#4, 5, 6) near the beginning of yellow-shaded strip. The following variations may be rather complex but usually initial positive jx pulse is followed by negative jx variation during the "yellow region".

First three events display the outward convection velocity ($VE_N > 0$ in panels *e*) throughout the event, suggesting that spacecraft usually encounters the expanding PSBL. With exception of time points showing large spikes or big differences between VTP and VTA results, the timing velocities also had large positive values, with VT > VE during most of the yellow region, as expected for active reconnection. According to ΔZN panel, the characteristic scales of discussed region could be a few tenth RE, they will be discussed in the next section.

Now we want to comment on the identification of the Hall-like (yellow) regions based on data shown in panels *f, g*. Here, during northern PSBL events, we aim to identify the regions with substantial Hall-like negative Ez and positive By components and we also look for correlated pairs –Ez/By and Ey/Bz as indication of possible Alfvén wave origin of these fields. Our identification of HR is primarily based on Ez variation rather than on its absolute value, which can be influenced by the choice of coordinate system and by other processes, like the wake effects. The appearance of these signatures differs in different events. The identification is obvious in the second and fourth cases (#5 and 6) in which we see a nice correlation in both pairs as well as large negative Ez of 4 and 8 m*V/m* peak amplitudes, correspondingly. In the first case (#4) the negative Ez variation of ~5 m*V/m* amplitude is superposed on top of large (up to 4 m*V/m*) + Ez from (possibly) wake interference effects, so here the absolute Ez values are obviously corrupted. Still the variations −δEz and +δBy are closely related to each other and they look similar on different spacecraft, so we tentatively identify it as the Hall-type region. The third case (#7) is different. Here we see the isolated −Ez spike down to −6 m*V/m*, so that Hall-type Ez is here. But unlike previous events, there is no visible correlation between electric and magnetic field components. So in this case the identification of yellow region is done based on Ez variation alone. This case is also different as regards the FAC behavior.

The quick survey of Figure 5 shows that the yellow region containing Hall-type E-signatures, sometimes being part of Alfvén wave-like perturbation, is associated with a number of profound changes of plasma properties in the PSBL. It is collocated with the appearance and development of energy-dispersed hot ion beams moving Earthward. It is closely associated with a remarkable change in the properties of cold ions, namely with a quick transformation of their narrow trace on the energy spectrogram to the diffuse trace which merges to the hot beam protons, indicating their heating. Being marked by the dashed green line in Figure 5, this time occurs in the second half of HR time interval. Finally, we notice that enhanced
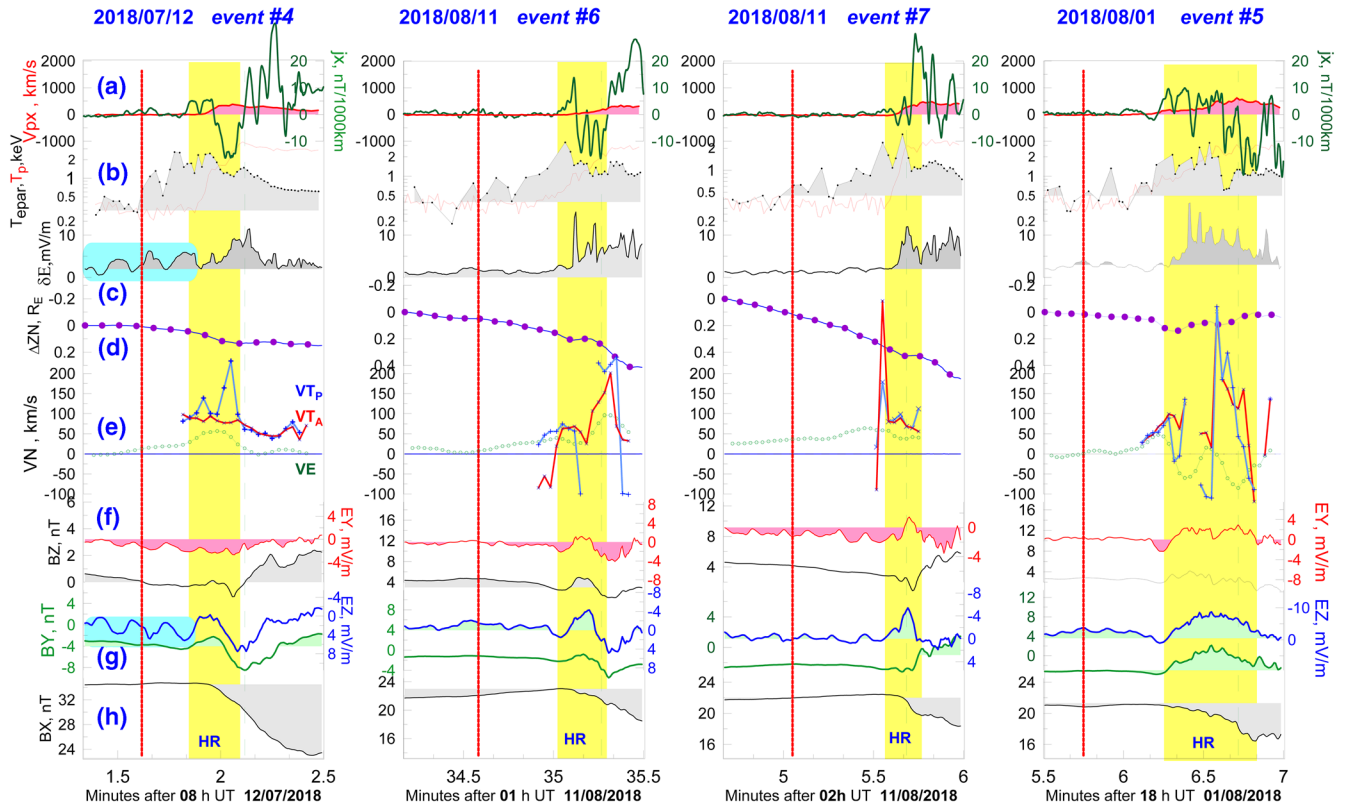
Figure 5. Survey of the mid-distance group of separatrix crossings. From top to bottom: Proton bulk flow (red) and jx (green) (a); parallel Te (black) and Tp (red) (b); variability δE from 32 Hz E-samples (c); ΔZN (d); normal components of convection and timing velocities (e); Bz and Ey (f), By and-Ez (g); Bx component (h). Onset of accelerated electron beam is shown by red vertical dotted line; dashed green line indicates the thermalization of cold ions; yellow vertical strip, labeled as HR, marks the time interval of intense Hall-type Ez variations, also. HR, Hall-type regions.

high-frequency and spiky E-fields (*c*) are also closely tied to the HR: they are absent throughout most of eSR before the HR onset, intensify during HR and may continue well into the high-beta outer plasma sheet region.

Next we evaluate quantitatively the episodes showing paired δE – δB correlations, which may indicate the Alfvén wave-related transport of Hall-type perturbation from the XNL to the observation point. In Figure 6, we show representative examples in four events, including observations made close to XNL (event #1), one of middle-distance events (#5) and two cases of distant XNL observations (events #8 and 9). We only analyze those portions of HR intervals which visually manifest the correlation, they are marked by yellow stripes in the Figure. For them, in the upper row we compare the 1 s increments y- and z-components of convection velocities $dVE_i = [dE \times B]_i/B^2$ inferred btom E- and B-field observations with their Alfvénic predictions $dVA_i = (dB_i/(\mu_0\rho))^{1/2}$. In event #1 we excluded an intense E-field spike (indicated by gray stripe on bottom panel). Because no similar E-spike was recorded at other spacecraft and because it had no associated magnetic counterpart, this spike is attributed to localized electrostatic high-amplitude potential drop, possibly, related to the e-hole.

The "Alfvén wave test" presented in Figure 6 shows that in two cases (1 and 9) the ratio δE/(δB V_A) is not far from 1. The larger values of regression slope (about 1.3) are found both in close (#1) and distant (#9) crossings, whereas rather low value ~0.3 was inferred in middle-distant crossing (#5). In the last case we had a gradual and long (~50 s) bay-like perturbation whose magnetic bay amplitude (dBy ~4–5 nT for dEz ~9 m*V/m*) was relatively large compared to other events. We emphasize that in two distant events the δE/ (δB V_A) test confirms the Alfvénic origin of analyzed large Ez variations. The large scatter of data points for #8 is basically contributed by large E-field spikes, possibly of electrostatic origin. The presented numerical
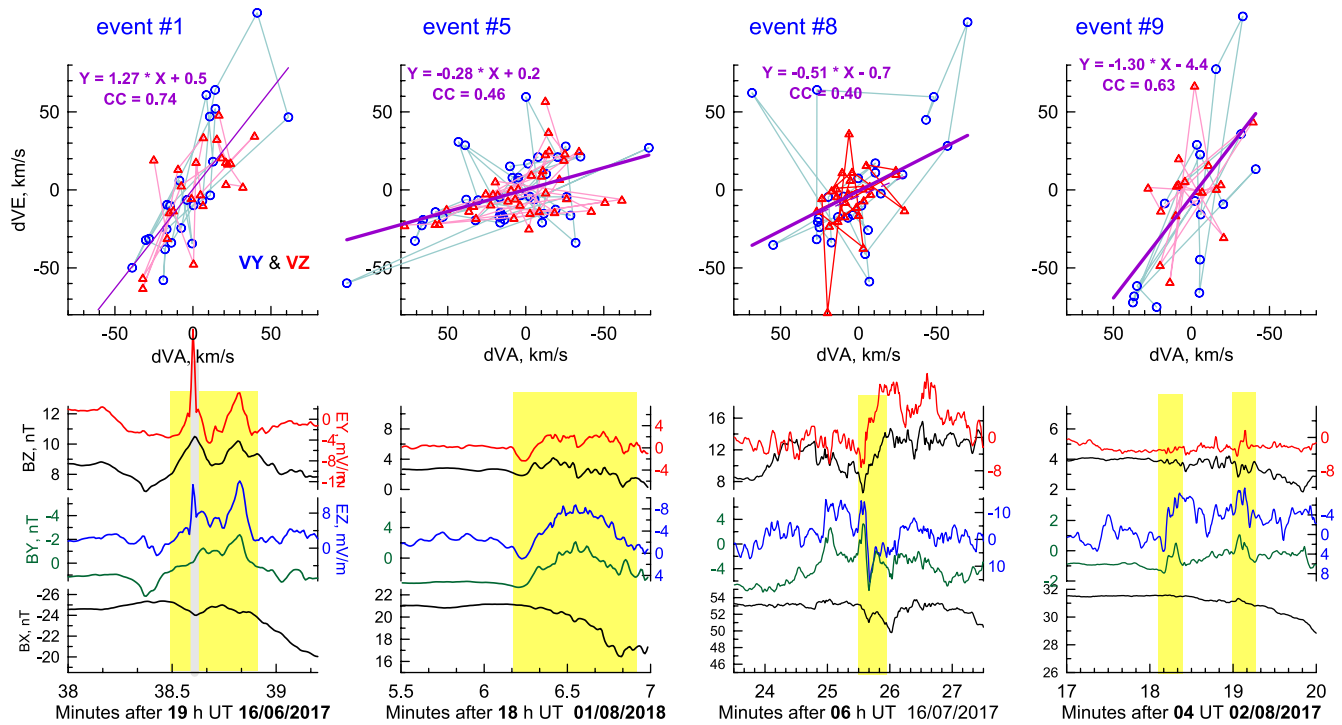
Figure 6. Alfvén tests for four intervals in the Hall-type region showing visually the anticorrelation between Ez and By variations. Bottom panels: illustration of B- and E- variations, yellow strip indicate the time intervals used in correlation study. Top panels: correlation plots between 1 s increments of observed y- and z-components of convection velocities dVE_i ($i = y,z$) with their Alfvénic prediction $dVA_i = (dB_i/(\mu_0\rho))^{1/2}$, linear regression results are also shown on the top.

values of Alfvén ratio should be considered as estimates because of some uncertainty of electron density values in the investigated low-density regions.

2.4. Survey of Distance Estimates and Other Parameters of Separatrix Crossings

In addition to Table S1 which provides a summary of nine events, in Figure 7, we summarize a few important characteristics of these events. The events are numbered according to their preliminary classification based on the observed particle signatures. So, the first three events were classified as closest events because they started from observation of tailward e-beam on electron spectrogram expected to be observed in the vicinity of the XNL (from them events #1 and #2 were presented in Figures 1 and 2). Next four mid-distance events ##4–7 started from Earthward accelerated electrons, they were summarized in Figure 5. Last two events #8 and #9, which showed a long-duration proton energy dispersion and other signatures of distant location of the XNL, were earlier presented in Figures 4 and 3, correspondingly.

The top panel (Figure 7a) illustrates the relative location of different boundaries along the normal to the current sheet. Like in previous sections, it was calculated as an integral of convection velocity along the normal to the current sheet as $\Delta Z_N = \int VE_N \, dt$, which is taken between the start-time of accelerated electrons (our proxy for magnetic separatrix encounter) and the time when the particular boundary was observed. For reference, for typical density in the lobe and outer RS region 0.05 cm^{-3} the ion inertial length d_i is about 1,000 km, which corresponds to the vertical grid size in Figure 7a. In addition to showing relative arrangement of boundaries, this Figure also provides the scale-size estimates of distances between different boundaries, providing that the 2D geometry is valid and the E-field estimates as well as the boundary orientation (N_{CS}) are accurate enough. One important boundary in this plot corresponds to the start of proton beam (P-beam, red). Its distance from magnetic separatrix ($\Delta Z_N = 0$) provides an estimate of the width of electron-part of reconnection separatrix region (eRS). This width is a fraction of d_i for events ##2–6 and about 1–2 d_i for #1 and 7. For distant events ##8, 9 the numbers are much larger, so for them we use the 5-times larger scale shown on the right side.
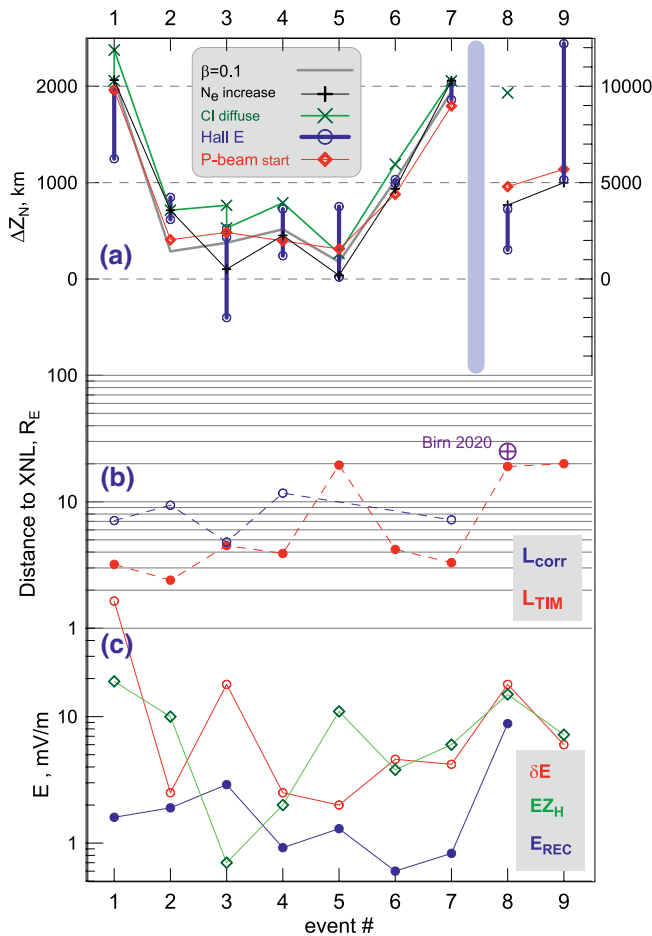
Figure 7. (a) Distance ΔZ_N perpendicular to B in the plasma frame between the registration of particular feature and initial location of magnetic separatrix (see text for more details); (b) MMS distance from the XNL estimated based on proton beam energy dispersion (red) and corrected for the velocity filter effect (blue, when possible); (c) peak amplitudes of characteristic E-field signatures, including the δE variability (red), Hall-type Ez (green), and reconnection rate estimate (E_{REC}, blue). Blue arrows in panel (b) indicate cases in which the convection filter correction is large but its magnitude cannot be determined accurately. MMS, magnetospheric multi-scale; XNL, X-type reconnection neutral line.

Next is the important region of intense Hall-type Ez field (shown by blue color here and by yellow strips in Figures 1–6) whose width is also a fraction of d_i. It is closely collocated with the P-beam which starts shortly before (#2, 6, and 7), inside (#4 and 5), or at the end (#1 and 3) of HR interval. Two gray-coded locations indicate where the electron density start to rise sharply above its lobe-like level and where the proton plasma beta parameter exceeds 0.1. These locations provide a marker relative to the plasma sheet structure, they stay close to the p-beam start and the Hall-type regions. Green symbols indicate the location where first signs of substantial thermalization of cold lobe ion beam can be noticed (such locations were also marked by green vertical lines in Figures 2–5). CI boundary is observed inside or short after the intense Hall-type Ez region signatures, this close correspondence may suggest that intense variable E-field in the Hall region contributes to the cold beam acceleration and thermalization. It is of note that frequently most of the Hall region consists of accelerated electrons and cold ion beams in addition to hot Earthward beam of energetic proton provided by the reconnection process.

In Figure 7b, we show the estimates of distance to the proton acceleration source, which is supposed to be the proxy for the distance to the active XNL. As illustrated by examples given in Figures 2–4, it was obtained from interpreting the energy-dispersed low-energy cutoff of energetic proton using the time-of-flight (TOF) model (see Wellenzohn et al., 2020 and Supplement 1). A so estimated distances L_{TOF} are available for all nine events, they are shown by red circles and range between 2 and >20 R_E in our data set (we warn that the result of TOF procedure depends on the choice of analyzed time interval, on the amount of energy channels selected and the thresholds used in low-energy cutoff determination, etc., therefore from our experience, the TOF results themselves are often accurate to within, say, a factor of 1.5). For event #8 an independent TOF estimate (provided in Figure 3 of Birn et al., 2020) was 25 R_E, as compared to our estimate of 19 R_E illustrated in Figure 4i. A relatively large distance (∼20 R_E) estimated in the event #5 looks as special feature rather than erroneous distance determination, because this event also manifests a very gradual appearance of ∼1 min-long bay-like perturbations and a low Alfvénic ratio (see Figures 4 and 6); which we do not fully understand at the moment.

As shown in Supplement 1, in the case of coexisting convection (VE) and separatrix velocity (supposed to be provided by observed timing velocity VT), the actual distance should be obtained as Lcorr = L_{TOF} VT/(VT−VE) (see Equation S4), where both velocities are taken along the normal to the current sheet. Obviously, our simple model suggests that convection is spatially homogeneous and time-stationary on the TOF timescale. Violation of this assumption (means, protons of different energies propagate at different velocities along the flux tube throughout spatially structured and propagated electric field) makes the task difficult and, we believe, this currently provides the main uncertainty to the separatrix velocity estimation. Another uncertainty sources are certainly the 2D geometry assumption, and the choice of normal direction. Because of these problems, and due to large variability of actual VE and VT, the correction procedure is more uncertain compared to the pure TOF estimate. As follows from Figure 7b, the correction factor may be rather large (up to a factor 4, event #2) or may have different signs in different parts of dispersed structure (in case of alternating outward or inward convection direction). In some cases, we failed to evaluate the correction factor due to either highly variable relationship between VT and VE (like in events #5 and 6 in Figure 5), or due to denominator (VT − VE) being close to zero (event #9, Figure 3).

Figure 7c surveys the characteristic values of electric field in the separatrix region. It includes the peak values of E-field differences recorded during 1 s time windows (δE, whose traces are particularly shown in Figure 5c) which generally characterize the LHD-scale wave activity with some contribution from E-spikes related to e-holes. Its typical values are of the order of 3–20 mV/m for all events in study, with similar amplitudes observed for distant events #8 and 9. The peak 1 s-average Hall Ez amplitudes (Ez_H, green color) are similarly strong. As discussed in Section 2.3 and shown in Figure 5g, small peak Ez absolute values in event #3 may not be representative of Hall effect because in this case large, ∼5 mV/m, negative Ez variation (which probably better characterizes the Hall field) started on top of large positive Ez background caused, presumably, by the wake effects.

This panel also includes the estimates of the reconnection rate, shown by blue color. They were obtained as $E_{REC} = (VT − VE)*B$ using 10 s sliding window for the time intervals including energy-dispersed ion beams, as illustrated in Figures 2–5. For most cases the reconnection rate is rather modest (about 1–2 mV/m), but the peak rate of ∼8 mV/m has been found during event #8 occurring during substorm expansion phase. Referring to Figure 4 we note that all other manifestations (electron energization up to ∼10 keV, very intense E-field and δE, FACs, etc) were also unusually strong during this PSBL crossing compared to other events. Such large reconnection rates of ∼10 mV/m have been previously found during highly disturbed events (e.g., Blanchard et al., 1997; T. K. M. Nakamura et al., 2018). With this comment in mind, the range of values of the reconnection rate (of order 0.1 if normalized to the lobe $V_A B$ values) found in our analyses is consistent with those which are typically found from observations, which supports the usefulness of reconnection rate estimation based on comparison of convection and timing velocities.

3. Discussion and Concluding Remarks

In this study, we basically confirm the main structural elements of reconnection-related separatrix region (SR), which are known from simulations and previous spacecraft studies. It includes electron-dominated region (EBL), energy-dispersed hot proton beam region (PBL) as well as Hall-polarity electric field Ez region (HR) which sometimes also displays associated Hall-polarity By-perturbations. Selection of brief PSBL crossings with confirmed reconnection signatures in particle data (replacement of lobe polar rain electrons by accelerated electron beams soon followed by Earthward energy-dispersed proton beams) proved to be a useful approach for that type of study. Additional evidence of ongoing reconnection was obtained from comparison of the timing velocity of magnetic structures (supposed to provide a proxy of separatrix motion) with the convective plasma velocity. Below we briefly summarize the finding and emphasize the inferred scales, amplitudes as well as differences related to different distances from the reconnection region and specific deviations from standard cartoons.

The low-density electron-dominated portion of separatrix region (EBL) in which accelerated electrons play a major role and ion population is present by cold lobe ions, is the PSBL outermost zone. The e-beams near magnetic separatrix, accelerated by the field-aligned E-field, have been shown in kinetic simulations of magnetic reconnection (e.g., Hesse et al., 2016, 2018, etc.). Previously they were identified in the magnetotail observations and discussed as the carriers of the lobeward part of the Hall current loop (Nagai et al., 2003; see a review by Paschmann et al., 2013). Such accelerated ∼keV-energy beams moving toward the XNL and accompanied by Earthward field-aligned current are observed near the magnetic separatrix in our events ##1–3 (Figure 1b and 1e). According to TOF distance estimates these events are closest to the XNL in our data set, being in the range of 3–5 R_E or 20–30 d_i, Figure 7b. No signatures of significant "toward e-beam" and positive j_x were recorded near magnetic separatrix in other 3 events observed at comparable distances from the XNL (##4, 6, 7), suggesting that this distance (∼30 d_i) may be near their visibility limit at the separatrix. An alternative explanation may be that "toward beams" are just intermittently observed. An interesting observation is that Earthward FACs and strong toward e-beam are often multiple and can be observed not only at the separatrix, but at some distance from it, for example, as deep as in the middle of IBL region (see, e.g., strong spike at 21:44 UT in event #2, Figure 1b).

Earthward-moving accelerated electrons are expected to belong to the electron-part of the reconnection outflow. When they are seen first time at the separatrix and throughout the entire EBL (##4, 6, and 7), the electron density does not show a significant increase and this continues throughout the EBL until the ion

beam arrival; this suggests some quasi-neutrality-related constraint. Instead, all crossings demonstrate the features of density depletions, down to a factor 2 or more against the lobe conditions. They are synchronously observed in electron density records as well as in the spacecraft potential variations (in cases when the ASPOC was off, like Figures 1–3). This is consistent with finding by Retinò et al. (2006) who found a density cavity adjacent to the separatrix at the distance estimated as 50 d_i (see also recent study by Yu et al., 2019).

Although it is not surprising that energetic electrons should be main current carriers in the EBL, it was very stimulating to observe systematically a high anticorrelation and amplitude correspondence between Vex and j_X variations in those cases when the ASPOC instrument was off. This detailed correspondence of variations continued throughout the HR and PBL regions—see Figures 1, 3, and 4. This confirms a good quality of curlometer results and allows us to use j_X as a substitute of Vex to conclude on the appearance of Earthward/tailward e-beams or flow bursts in many those events, in which the FPI flow measurements were uncertain (in our practice, this occurred in tenuous lobe-like density regions when the ASPOC was on). In observations we typically meet multiple FAC sheets, often with the alternating polarities, throughout the Hall regions and, sometimes, in the EBL region; they often continue well into the plasma sheet. As it was mentioned, in middle-distance events of Figure 5 (estimated to be at 30–50 d_i from the XNL) the downward FAC (corresponding to tailward electron flow) is observed not right at the "magnetic separatrix" but at some distance from it, inside the Hall region; similar feature was also reported by Varsani et al. (2017) for the storm-time substorm. Once more, one has to mention that we discuss the mesoscale picture whereas plenty of subsecond FAC structures have been also observed in the separatrix region (e.g., Alm et al., 2018; R. Nakamura et al., 2016, etc.).

It is interesting that electron characteristic energy (Tepar) often reaches its peak in the outermost half of Hall region and that this energy is often comparable to the average proton energy when the proton beam appears. This feature of separatrix region, also noticed in Varsani et al. (2017) and Yu et al. (2019) papers, is different from observations in the central plasma sheet region where Tp/Te ∼5–10. The enhanced electron energy in EBL is not reproduced in the Cluster statistical survey (Walsh et al., 2011) suggesting that it is a feature of just reconnection events.

The most interesting part of separatrix region is probably the 'Hall-like' region (HR). The HR width across-B, according to Figure 7a is also less than a proton inertial length for events at 20–50 d_i distances. As already noticed in Section 2.3, the HR is associated with a number of profound changes of plasma properties in the PSBL. It usually overlaps with the region of energy-dispersed hot ion beams moving Earthward, it is closely associated with the heating of cold ion beams, it also hosts strongest Ez and FAC magnitudes as well as enhanced high-frequency and spiky E-fields which are not investigated in much detail in our study.

Inspection of Figures 2–5 indicates that some portions of the yellow region, which represents intense Hall-like Ez-signature, often contain correlated δE and δB variations consistent with the Alfvén-type perturbation. In these few cases the estimates of Alfvénic ratio δE/(δB V_A) varied between 0.3 and 1.3 (Section 2.3, Figure 6) indicating that the δE/δB value is an order of the Alfvén velocity, which is as high as ∼2,000 km/s for B = 20 nT and Ne = 0.05 cm^{-3}. Different from large amplitude δE variation, in such low-**density conditions the Alfvénic δB variations are weak, a few nT at most. As they are often observed on top of relatively strong variations imposed by some other meso- and large-scale FAC structures, this makes difficult their extraction and analyses.

There was a discussion in the literature as concerns the role of kinetic Alfvén waves (KAW) in reconnection. They were identified in some PIC simulations in the vicinity of the separatrices and related to ion diffusion region Hall fields (e.g., Dai et al., 2017; Huang et al., 2018; Shay et al., 2011) argued that Alfvén-wave polarity magnetic and electric perturbations can be transported along magnetic field lines to a large distance, this was also confirmed in a 3D global hybrid simulation of magnetotail reconnection (Cheng et al., 2020). On the observational side, the KAW were identified in the proximity of reconnection line (Chaston et al., 2009) as well as in the plasma sheet (Chaston et al., 2012), although their relationship to PSBL structure and separatrix was not specifically addressed. Duan et al. (2016) reported KAW-like phenomena observed in the PSBL by THEMIS at ∼10 R_E at the substorm onset. Particularly, they demonstrated very intense Ez pulses of Hall-type polarity (southward δEz up to 30 mV/m and duskward δBy) with δE/δB ratio for the pulses in the range of 2,000–6,000 km/s (Alfvénic ratio >>1) accompanied by tailward keV e-beam and downward

FAC. These strong perturbations provided a large downward Poynting flux sufficient to cause the auroral brightening.

We would like to add the following observations to the continuing KAW discussions. We remind that HR meridional size across the magnetic field line is small, less than proton inertial length for close and mid-distance crossings in Figure 7a, which is discussed as one of the requirements for KAW. However, as regards the Alfvénic ratio which is expected to be >>1 in the KAW, in most of our correlating δE, δB events it is not that large. This does not exclude that some sharp variation fronts may have larger ratio required by KAW model, suggesting that only very localized portions of entire HR region may be associated with propagating KAW. Second, there are obvious examples showing intense Hall-polarity δEz variations being not accompanied by δBy, like in the event #7 in Figure 5; or that HR portions with correlating and non-correlating δE, δB coexist spatially. Strong time-dependence of the reconnection rate and/or interaction of Earthward-propagating AW with dipole-like field and ionosphere certainly can complicate the picture. Anyway the situations look more complicated, and requires more investigation.

The region of energy-dispersed proton beam (PBL) is where the density as well as plasma beta grows from lobe-like values toward their plasma sheet values, this seems to be valid for nearby, mid-distance, and for distant PSBL crossings as well. It is of interest that in all our cases the cold ion beam trace coexists with hot ion beam throughout most of dispersed hot beam region (including two distant events) as well as throughout most of HR region; similar observations were previously published by (Alm et al., 2018; Varsani et al., 2017; Wellenzohn et al., 2020). Besides ion acceleration in the proximity of the XNL, Nagai et al. (2015) also discussed another way of ion acceleration: that cold ions convect inward and undergo the acceleration in strong Hall Ez regions during inflow and then they are further accelerated to form the ion outflows in the wide range of energies. Indeed, in Figures 2–4, we clearly see a significant increase of cold beam energy caused by the enhanced convection. However, whereas for heavy ions this acceleration can be very significant, for protons, which are predominantly observed in our cases during solar minimum conditions, the convective energies are not that high, being usually below a few 100 s eV, or up to 1 keV like in the most active event shown in Figure 4. The thermalization of cold ion beam can only contribute to the low-energy part of plasma sheet ion spectra.

The spatial ordering pattern in which the EBL (the outmost layer) is followed by HR and IBL regions can naturally be understood in terms of the same velocity filtering process which forms the energy-dispersed low energy cutoff of hot ion beams and electron beams (see Varsani et al., 2017; Wellenzohn et al., 2020 for illustration of consistency of p- and e-beams dispersion). Indeed, the Alfvén velocity (say, ~2,000 km/s) near the separatrix is usually much smaller compared to the thermal velocity of accelerated electrons, but it is of the same order of magnitude compared to proton beam velocity (2,000 km/s for 25 keV proton). This explains the fact that HR significantly overlaps with the energy-dispersed hot ions beam region and that both of them are similarly displaced inward from the magnetic separatrix—see Figure 7a. The same ordering is also seen in the distant crossings presented in Figures 3 and 4, and such ordering can possibly be mapped along the flux tube down to the low altitude. This follows from results by Sauvaud et al. (1999) who found that transient energy-dispersed proton beam injections at ~2R_E altitude are seen together with strong shear Alfvén waves, whose highest amplitude was observed near the poleward front of expanding auroral bulge during substorms.

Next we discuss - how similar is the SR structure observed in the near- to middle-distance events (at distances ≤ 50 d_i) comparing to two distant SR crossings, supposed to be at the distances exceeding 20R_E (or >>100 d_i) as discussed in Section 2.4. Morphologically, SR structure in both groups is surprisingly similar: it has the outermost EBL region with low lobe-like density and density depletions; very distinct HR region (with intense Hall-like Ez field and Alfvénic By variations), energy-dispersed hot proton beam (PBL), with cold ion traces across the EBL, HR and PBL regions. At the same time the temporal and spatial scales of these regions are very different. The residence time in the EBL as well as the durations of HR and PBL region crossings are as long as 1–2 min. Whereas typical EBL width across B is estimated to be above a fraction of d_i (≤1,000 km) in events ##1–7, in distant cases #8 and 9 it could be as large as ~5,000 km according to the integrated convection flow (note that an expanding scale is used on the right side of Figure 7a for events #8 and 9). We emphasize that in the most distant crossing #9, the convection component along the current sheet normal was stable throughout the entire SR crossing, suggesting that upward plasma convection had

a large-scale nature and that convection-based scale estimate is robust in this case. This big scale difference between middle-distance and distant crossings is not surprising, because both the TOF scale and estimated vertical distance from the separatrix should be scaled as the distance from the XNL if we adopt the velocity filtering picture discussed above. In that sense the velocity-related eBL, pBL, and HR ordering provides a strong support to the Alfvénic origin of Hall-polarity strong Ez field observed at large distances from the reconnection line. Penetration into the plasma sheet of the intense KAW during its Earthward propagation from the reconnection source was recently demonstrated in a 3D global hybrid simulation of magnetotail reconnection (Cheng et al., 2020).

Finally, we also notice that the observed SR structure does not fully fit to idealized reconnection cartoons so that we notice some systematic deviations from a simple picture. For example, unlike the suggestion, that the Hall current system near the separatrix layer is formed by a thin double-sheet (mostly FAC) structure (e.g., Nagai et al., 2003), we always observe multiple FAC sheets of alternating polarities which are met in the EBL region (sometimes) and Hall regions (always), and which often continues well into the plasma sheet. Also, strong Hall-type Ez region is very structured and its Alfvén-like portions neighbor with its parts showing no correlation between δEz and δBy. One factor contributing to this complexity is the intrinsic impulsive nature of magnetotail reconnection which is well-known from both observations (e.g., Baumjohann et al., 1989; Sauvaud et al., 1999) and simulations (e.g., Hesse et al., 2016; Wiltberger et al., 2015). Additional factors can be the occasional multiplicity of active reconnection sites and interaction of reconnection outflows with dipolarized region of plasma sheet and the inner magnetosphere. Dedicated simulations are required to understand specific influences of these factors on the separatrix region structure.

Data Availability Statement

The MMS data are publically available via NASA resources and the Science Data Center at CU/LASP (https://lasp.colorado.edu/mms/sdc/public/).

References

Alexeev, I. V., Sergeev, V., Owen, C. J., Fazakerley, A., Lucek, E., & Re´me, H. (2006). Remote sensing of a magnetotail reconnection X-line using polar rain electrons. *Geophysical Research Letters*, *33*, L19105. https://doi.org/10.1029/2006GL027243

Alm, L., Andre, M., Vaivads, A., Khotyaintsev, Y. V., Torbert, R. B., & Burch, J. L. (2018). Magnetotail Hall physics in the presence of cold ions. *Geophysical Research Letters*, *45*, 10941–10950. https://doi.org/10.1029/2018GL079857

Baumjohann, W., Paschmann, G., & Cattell, C. A. (1989). Average plasma properties in the central plasma sheet. *Journal of Geophysical Research*, *94*(A6), 6597–6606. https://doi.org/10.1029/JA094iA06p06597

Birn, J., Chandler, M., & Nakamura, R. (2020). Ion beams in the plasma sheet boundary layer: MMS observations and test particle simulations. *Journal of Geophysical Research: Space Physics*, *125*, e2019JA027113. https://doi.org/10.1029/2019JA027113

Blanchard, G. T., Lyons, L. R., & de la Beaujardière, O. (1997). Magnetotail reconnection rate during magnetospheric substorms. *Journal of Geophysical Research*, *102*(A11), 24303–24312. https://doi.org/10.1029/97JA02163

Burch, J. L., Moore, T. E., Torbert, R. B., & Giles, B. L. (2015). Magnetospheric multiscale overview and science objectives. *Space Science Reviews*, *199*, 5–21. https://doi.org/10.1007/s11214-015-0164-9

Chaston, C. C., Bonnell, J. W., Clausen, L., & Angelopoulos, V. (2012). Energy transport by kinetic-scale electromagnetic waves in fast plasma sheet flows. *Journal of Geophysical Research*, *117*, A09202. https://doi.org/10.1029/2012JA017863

Chaston, C. C., Johnson, J. R., Wilber, M., Acuna, M., Goldstein, M. L., & Reme, H. (2009). Kinetic Alfvén wave turbulence and transport through a reconnection diffusion region. *Physical Review Letters*, *102*, 015001. https://doi.org/10.1103/PhysRevLett.102.015001

Cheng, L., Lin, Y., Perez, J. D., Johnson, J. R., & Wang, X. (2020). Kinetic Alfvén waves from magnetotail to the ionosphere in global hybrid simulation associated with fast flows. *Journal of Geophysical Research: Space Physics*, *125*, e2019JA027062. https://doi.org/10.1029/2019JA027062

Dai, L. (2009). Collisionless magnetic reconnection via Alfven eigenmodes. *Physical Review Letters*, *102*, 245003. https://doi.org/10.1103/PhysRevLett.102.245003

Dai, L., Wang, C., Zhang, Y., Lavraud, B., Burch, J., Pollock, C., et al. (2017). Kinetic Alfvén wave explanation of the Hall fields in magnetic reconnection. *Geophysical Research Letters*, *44*, 634–640. https://doi.org/10.1002/2016GL071044

Duan, S. P., Dai, L., Wang, C., Liang, J., Lui, A. T. Y., Chen, L. J., & He, Z. H. (2016). Evidence of kinetic Alfvén eigenmode in the near-Earth magnetotail during substorm expansion phase. *Journal of Geophysical Research: Space Physics*, *121*, 4316–4330. https://doi.org/10.1002/2016JA022431

Eastwood, J. P., Phan, T. D., Øieroset, M., & Shay, M. A. (2010). Average properties of the magnetic reconnection ion diffusion region in the Earth's magnetotail: The 2001–2005 Cluster observations and comparison with simulations. *Journal of Geophysical Research*, *115*, A08215. https://doi.org/10.1029/2009JA014962

Ergun, R. E., Tucker, S., Westfall, J., Goodrich, K. A., Malaspina, D. M., Summers, D., & Wallace, J. (2014). The Axial Double Probe and Fields Signal Processing for the MMS Mission. *Space Science Reviews*, *199*, 167–188. https://doi.org/10.1007/s11214-014-0115-x

Grigorenko, E. E., Runov, A., Angelopoulos, V., & Zelenyi, L. M. (2019). Particle beams in the vicinity of magnetic separatrix according to near-lunar ARTEMIS observations. *Journal of Geophysical Research: Space Physics*, *124*, 1883–1903. https://doi.org/10.1029/2018JA026160

Haaland, S., Lybekk, B., Maes, L., Laundal, K., Pedersen, A., Tenfjord, P., et al. (2017). North-south asymmetries in cold plasma density in the magnetotail lobes: Cluster observations. *Journal of Geophysical Research: Space Physics*, *122*, 136–149. https://doi.org/10.1029/2016JA023404

Hesse, M., Aunai, N., Birn, J., Cassak, P., Denton, R. E., Drake, J. F., et al. (2016). Theory and modeling for the magnetospheric multiscale mission. *Space Science Reviews*, *199*(1), 577. https://doi.org/10.1007/s11214-014-0078-y

Hesse, M., Norgren, C., Tenfjord, P., Burch, J. L., Liu, Y.-H., Chen, L.-J., et al. (2018). On the role of separatrix instabilities in heating the reconnection outflow region. *Physics of Plasmas*, *25*, 122902. https://doi.org/10.1063/1.5054100

Huang, H., Yu, Y., Dai, L., & Wang, T. (2018). Kinetic Alfven waves excited in two-dimensional magnetic reconnection. *Journal of Geophysical Research: Space Physics*, *123*, 6655–6669. https://doi.org/10.1029/2017JA025071

Keiling, A., Rème, H., Dandouras, I., Bosqued, J. M., Parks, G. K., McCarthy, M., & Lundin, R. (2004). Transient ion beamlet injections into spatially separated PSBL flux tubes observed by Cluster-CIS. *Geophysical Research Letters*, *31*, L12804. https://doi.org/10.1029/2004GL00272

Khotyaintsev, Y. V., Graham, D. B., Norgren, C., & Vaivads, A. (2019). Collisionless magnetic reconnection and waves: Progress review. *Frontiers in Astronomy and Space Science*, *6*, 70. https://doi.org/10.3389/fspas.2019.00070

Lapenta, G., R. Wang, E. Cazzola (2016), Reconnection Separatrix: Simulations and spacecraft measurements. In '*Magnetic reconnection: Concepts and applications*' W. Gonzalez and E. Parker, (Eds), Astrophys. and space sci library, Springer, (pp 315–344).

Lindqvist, P.-A., Olsson, G., Torbert, R. B., King, B., Granoff, M., Rau, D. M., & Needell, G. (2014). The Spin-Plane Double Probe Electric Field Instrument for MMS. *Space Science Reviews*, *199*, 137–165. https://doi.org/10.1007/s11214-014-0116-9

Nagai, T., Shinohara, I., Fujimoto, M., Machida, S., Nakamura, R., Saito, Y., & Mukai, T. (2003). Structure of the Hall current system in the vicinity of the magnetic reconnection site. *Journal of Geophysical Research*, *108*, 1357. https://doi.org/10.1029/2003JA009900

Nagai, T., Shinohara, I., & Zenitani, S. (2015). Ion acceleration processes in magnetic reconnection: Geotail observations in the magnetotail. *Journal of Geophysical Research: Space Physics*, *120*, 1766–1783. https://doi.org/10.1002/2014JA020737

Nakamura, T. K. M., Nakamura, R., Varsani, A., Genestreti, K. J., Baumjohann, W., & Liu, Y. –. H. (2018). Remote sensing of the reconnection electric field from in-situ multipoint observations of the separatrix boundary. *Geophysical Research Letters*, *45*, 3829–3837. https://doi.org/10.1029/2018GL078340

Nakamura, R., Sergeev, V. A., Baumjohann, W., Plaschke, F., Magnes, W., Fischer, D., & Varsani, A. (2016). Transient, small-scale field-aligned currents in the plasma sheet boundary layer during storm time substorms. *Geophysical Research Letters*, *43*(10), 4841–4849. https://doi.org/10.1002/2016GL068768

Øieroset, M., Phan, T. D., Fujimoto, M., Lin, R. P., & Lepping, R. P. (2001). In situ detection of collisionless reconnection in the Earth's magnetotail. *Nature*, *412*, 414–417. https://doi.org/10.1038/35086520

Onsager, T. G., Thomsen, M. F., Gosling, J. T., & Bame, S. J. (1990). Electron distributions in the plasma sheet boundary layer: Time-of-flight effects. *Geophysical Research Letters*, *17*(11), 1837–1840. https://doi.org/10.1029/GL017i011p01837

Parks, G., Chen, L. J., McCarthy, M., Larson, D., Lin, R. P., & Phan, T., et al. (1998). New observations of ion beams in the plasma sheet boundary layer. *Geophysical Research Letters*, *25*, 3285. https://doi.org/10.1029/98GL02208

Paschmann, G., Øieroset, M., & Phan, T. (2013). In-situ observations of reconnection in space. *Space Science Reviews*, *178*, 385–417.

Plaschke, F., Kahr, N., Fischer, D., Nakamura, R., Baumjohann, W., Magnes, W., & Burch, J. L. (2016). Steepening of waves at the duskside magnetopause. *Geophysical Research Letters*, *43*, 7373–7380. https://doi.org/10.1002/2016GL070003

Pollock, C., Moore, T., Jacques, A., Burch, J., Gliese, U., Saito, Y., & Omoto, T. (2016). Fast plasma investigation for magnetospheric multiscale. *Space Science Reviews*, *199*, 331–406. https://doi.org/10.1007/s11214-016-0245-4

Retinò, A., Vaivads, A., André, M., Sahraoui, F., Khotyaintsev, Y., Pickett, J. S., & Bavassano Cattaneo, M. B. (2006). Structure of the separatrix region close to a magnetic reconnection X-line: Cluster observations, *Geophysical Research Letter*, *33*, L06101. https://doi.org/10.1029/2005GL024650

Russell, C. T., Anderson, B. J., Baumjohann, W., Bromund, K. R., Dearborn, D., Fischer, D., & Le, G. (2014). The magnetospheric multiscale magnetometers. *Space Science Reviews*, *199*, 89–256. https://doi.org/10.1007/s11214-014-0057-3

Sauvaud, J.-A., & Kovrazhkin, R. A. (2004). Two types of energy-dispersed ion structures at the plasma sheet boundary. *Journal of Geophysical Research*, *109*, A12213. https://doi.org/10.1029/2003JA010333

Sauvaud, J.-A., Popescu, D., Delcourt, D. C., Parks, G. K., Brittnacher, M., Sergeev, V. A., & Kovrazhkin, R. A. (1999). Sporadic plasma sheet ion injections into the high altitude auroral bulge: Satellite observations. *Journal of Geophysical Research*, *104*, 28. https://doi.org/10.1029/1999JA900293.565

Shay, M. A., Drake, J. F., Eastwood, J. P., & Phan, T. D. (2011). Super-Alfvénic Propagation of Substorm Reconnection Signatures and Poynting Flux. *Physical Review Letters*, *107*, 065001. https://link.aps.org/doi/10.1103/PhysRevLett.107.065001

Shirai, H., Maezawa, K., Fujimoto, M., Mukai, T., Yamamoto, T., Saito, Y., Kokubun, S., & Kaya, N. (1997). Drop-off of the polar rain flux near the plasma sheet boundary. *Journal of Geophysical Research*, *102*(A2), 2271–2278. https://doi.org/10.1029/96JA02600

Takahashi, K., & Hones, E. W. (1988). ISEE 1 and 2 observations of ion distributions at the plasma sheet-tail lobe boundary. *Journal of Geophysical Research*, *93*, 8558. https://doi.org/10.1029/JA093iA08p08558

Tsyganenko, N. A., & Andreeva, V. A. (2015). A forecasting model of the magnetosphere driven by an optimal solar-wind coupling function. *Journal of Geophysical Research: Space Physics*, *120*, 8401–8425. https://doi.org/10.1002/2015JA021641

Varsani, A., Nakamura, R., Sergeev, V. A., Baumjohann, W., Owen, C.J., Petrukovich, A. A., & Yao, Z. (2017). Simultaneous remote observations of intense reconnection effects by DMSP and MMS spacecraft during a storm time substorm. *Journal of Geophysical Research: Space Physics*, *122*. https://doi.org/10.1002/2017JA024547

Walsh, A. P., Owen, C. J., Fazakerley, A. N., Forsyth, C., & Dandouras, I. (2011). Average magnetotail electron and proton pitch angle distributions from Cluster PEACE and CIS observations. *Geophysical Research Letters*, *38*, L06103. https://doi.org/10.1029/2011GL046770

Wellenzohn, S., Nakamura, R., Nakamura, T. K. M., Varsani, A., Sergeev, V., Apatenkov, S., et al. (2020). Remote sensing of magnetic reconnection in the magnetotail using in situ multipoint observations at the plasma sheet boundary layer. *Journal of Geophysical Research: Space Physics*, *125*. https://doi.org/10.1029/2020JA028917

Wiltberger, M., Merkin, V., Lyon, J. G., & Ohtani, S. (2015). High-resolution global magnetohydrodynamic simulation of bursty bulk flows. *Journal of Geophysical Research: Space Physics*, *120*(6), 4555–4566. https://doi.org/10.1002/2015JA021080

Yu, X., Wang, R., Lu, Q., Russell, C. T., & Wang, S. (2019). Nonideal electric field observed in the separatrix region of a magnetotail reconnection event. *Geophysical Research Letters*, *46*, 10744–10753. https://doi.org/10.1029/2019GL082538

Zelenyi, L. M., Kovrazkhin, R. A., & Bosqued, J. M. (1990). Velocity-dispersed ion beams in the nightside auroral zone: Aureol 3 observations. *Journal of Geophysical Research*, *95*(A8), 12119–12139. https://doi.org/10.1029/JA095iA08p12119